



Contents lists available at ScienceDirect

## Thin Solid Films

journal homepage: [www.elsevier.com/locate/tsf](http://www.elsevier.com/locate/tsf)Properties of atomic layer deposited HfO<sub>2</sub> thin filmsJustin C. Hackley<sup>1</sup>, Theodosia Gougousi\*

Department of Physics, University of Maryland, Baltimore County (UMBC), Baltimore, MD 21250, USA

## ARTICLE INFO

## Article history:

Received 22 September 2008

Received in revised form 25 February 2009

Accepted 13 April 2009

Available online 19 April 2009

## Keywords:

Atomic layer deposition

Hafnium oxide

Infrared spectroscopy

XRD

Refractive index

## ABSTRACT

The growth, composition and morphology of HfO<sub>2</sub> films that have been deposited by atomic layer deposition (ALD) are examined in this article. The films are deposited using two different ALD chemistries: i) tetrakis ethylmethyl amino hafnium and H<sub>2</sub>O at 250 °C and ii) tetrakis dimethyl amino hafnium and H<sub>2</sub>O at 275 °C. The growth rates are 1.2 Å/cycle and 1.0 Å/cycle respectively. The main impurities detected both by X-ray Photoelectron Spectroscopy and Fourier transform infrared spectroscopy (FTIR) are bonded carbon (~3 at.%) and both bulk and terminal OH species that are partially desorbed after high temperature inert anneals up to 900 °C. Atomic Force Microscopy reveals increasing surface roughness as a function of increasing film thickness. X-ray diffraction shows that the morphology of the as-deposited films is thickness dependent; films with thickness around 30 nm for both processes are amorphous while ~70 nm films show the existence of crystallites. These results are correlated with FTIR measurements in the far IR region where the HfO<sub>2</sub> peaks are found to provide an easy and reliable technique for the determination of the crystallinity of relatively thick HfO<sub>2</sub> films. The index of refraction for all films is very close to that for bulk crystalline HfO<sub>2</sub>.

© 2009 Elsevier B.V. All rights reserved.

## 1. Introduction

Hf-based dielectrics are the leading contenders for the replacement of Si-based gate oxides in Metal Oxide Semiconductor Field Effect Transistors and as insulating dielectrics in memory devices. The electrical and interface properties of Hf-based thin films deposited on Si, Ge and compound semiconductors by an assortment of physical and chemical techniques have been studied extensively in the past decade. [1–7] Due to their high refractive index ranging from 1.8 to 2.2 and low absorption, [8] thicker HfO<sub>2</sub> films are used for the production of optical multilayer coatings for ultraviolet to infrared applications [8–10]. In combination with SiO<sub>2</sub> they are used to form multilayers with high laser induced damage threshold [10]. The hardness and thermal stability exhibited by HfO<sub>2</sub> films also make them useful as protective coatings, [11–13] and in coatings for heat mirrors. [14] Such coatings are usually produced by electron-beam evaporation or sputtering. [8,10,15].

In this work, HfO<sub>2</sub> films with thickness in excess of 10 nm are grown by Atomic Layer Deposition (ALD) on Si substrates using two different, though similar, chemistries utilizing amide precursors and H<sub>2</sub>O. ALD is a thin film deposition technique that is based on a self-limiting, complementary surface reaction scheme [16]. It produces smooth, conformal films even over high aspect ratio topography and permits excellent thickness control [17]. The films' surface and bulk morphology, index of refraction and purity are examined by X-ray

Photoelectron Spectroscopy (XPS), Fourier transform infrared spectroscopy (FTIR), spectroscopic ellipsometry (SE), X-ray Diffraction (XRD) and Atomic Force Microscopy (AFM) as a function of thickness and post deposition thermal treatment.

## 2. Experimental details

The films were deposited in a home-built hot-wall flow type ALD reactor, computer-controlled via a Labview<sup>®</sup> routine [2]. Both amide precursors were purchased from Sigma-Aldrich in a sealed glass ampoule and transferred to a stainless steel vessel in a nitrogen atmosphere to avoid decomposition. The precursor container was then attached to a modular delivery system that was placed in an oven to ensure uniform heating of all surfaces and lines. H<sub>2</sub>O was used as the oxidizing agent. The air and or nitrogen were removed from the storage vessels using several freeze, pump, and thaw cycles at appropriate temperatures. Both reagents were delivered using the fixed volume approach described by Hausmann et al. [18]. To ensure sufficient vapor pressure the tetrakis dimethyl amino hafnium (TDMAHf) container was heated to 70 °C, the tetrakis ethylmethyl amino hafnium (TEMAHf) vessel was maintained at 105 °C and the water vessel was kept at room temperature. The films examined in this work were deposited either on native oxide or HF etched (Si–H) Si (100) substrates.

Film thickness was measured using fixed-angle (70°) spectroscopic ellipsometry (SE) at 380–900 nm, and the values reported represent the mean of five measurements over a typical sample size of 1.5 × 1.5 cm. The index of refraction was extracted from the ellipsometry measurements assuming a Cauchy dispersion model.

\* Corresponding author.

E-mail address: [gougousi@umbc.edu](mailto:gougousi@umbc.edu) (T. Gougousi).<sup>1</sup> Current address: Laboratory for Physical Sciences, 8050 Greenmead Drive, College Park, MD 20740, United States.

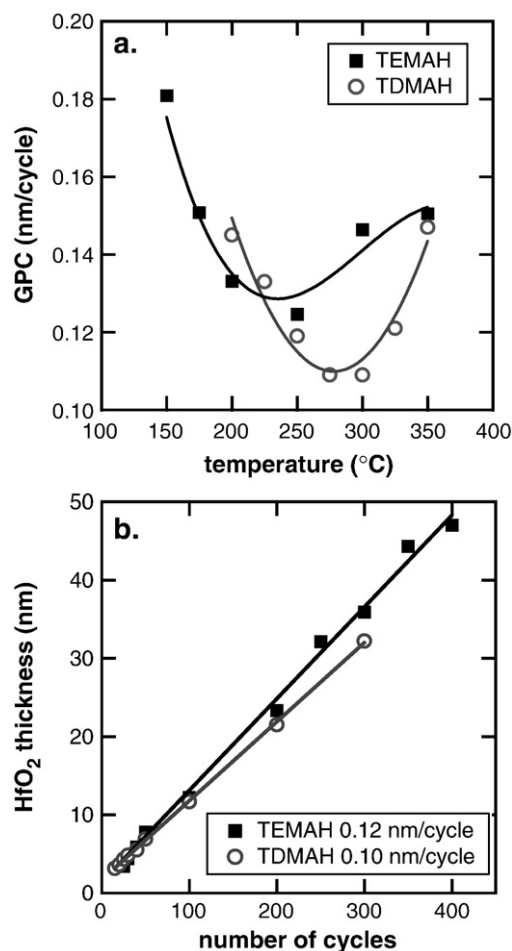


**Fig. 1.** a) The growth rate per cycle (GPC) for the two ALD processes. For the TEMAHf chemistry the ALD minimum is reached at 250 °C and for the TDMAHf process is reached at 275 °C. The solid lines are intended as a guide to the eye. b). Film thickness as a function of ALD cycle number. The depositions were performed at 250 °C with TEMAHf and 275 °C for TDMAHf.

XPS analysis of the samples was performed *ex situ* by Kratos Ultra XPS spectrometers at 0° takeoff-angle with 0.5 eV step size for survey scans and 0.1 eV step size for high-resolution scans using an Al achromatic source,  $h\nu = 1486.6$  eV. The energy scale was calibrated against the C 1s peak that was set at 285 eV. The samples were not sputter cleaned prior to analysis. FTIR was performed in the mid and far infrared region using a Thermo Nicolet 4700 FTIR bench in the transmission mode. In the mid IR region a deuterated L-alanine doped triglycine sulphate (DLATGS) detector with KBr window and KBr beam splitter was used. In the far IR region a DLATGS detector with Polyethylene window ( $700\text{--}50\text{ cm}^{-1}$ ) and solid substrate beam splitter was used. A resolution of  $4\text{ cm}^{-1}$  with 256 scans was used for all acquisitions. A background spectrum was taken before each set of measurements; the transmission spectrum acquired for each sample was then referenced to the background to give an absorbance spectrum. A filtration system was installed on the inlet of the purge line to remove CO<sub>2</sub>, moisture and particulates from the purge air. Samples were annealed for 2 min in Ar either in a Heatpulse or an ULVAC MILA rapid thermal annealer (RTA).

Film crystallization was examined using a Philips X'Pert X-Ray Diffractometer (XRD) for the TEMAHf samples, and a Siemens D500S XRD system for the TDMAHf samples. AFM data was collected with a Thermo Microscope Autoprobe instrument in the contact mode. Some samples were analyzed with a Digital Instruments 3100 instrument in the tapping mode. Typical scan sizes were  $1\text{--}2\ \mu\text{m}^2$  and data were acquired at 1 Hz scanning rate. Both the vendor software and WSxM

2.2 Scanning Probe Microscopy software were used to process and display the AFM images [19].

### 3. Results and discussion

#### 3.1. Growth rate and process temperature

SE has been used to determine the ALD window [17] and the growth rate under optimal ALD conditions. Fig. 1a shows the growth per cycle (GPC) for each process on a Si native oxide surface as a function of substrate temperature. The GPC vs. temperature curve for both precursors exhibits a rather steep parabolic profile rather than a plateau and the ALD minimum was found at 250 °C for the TEMAHf process and at 275 °C for the TDMAHf process, and these process temperatures were used in this work. Fig. 1b shows the film thickness as a function of process cycle number. The growth rate is  $1.2\ \text{\AA}/\text{cycle}$  for the TEMAHf process and  $1.0\ \text{\AA}/\text{cycle}$  for the TDMAHf process, comparable to growth rates reported for similar processes [20–23]. The difference in the growth rate for the two precursors may originate from the slight difference in the deposition temperature. Fig. 1a shows that at 250 °C the GPC for TDMAHf is comparable to the GPC for TEMAHf.

#### 3.2. Film composition

XPS was used to analyze the film composition and the results are displayed on Table 1 [24]. For both processes no bonded nitrogen was detected in the films and the bonded carbon content is  $\sim 3$  at.%. Within the uncertainty of the measurement the films produced by both precursors were stoichiometric with the films produced with TDMAHf slightly more oxygen rich (O/Hf  $\sim 2.2$ ). The films were exposed to air prior to the compositional analysis and it is possible that some of the bonded carbon and oxygen may have resulted from reactions with atmospheric carbon dioxide and moisture [25]. As a result, the bonded carbon and oxygen film content should be regarded as an upper limit.

The presence of impurities on the film surface was examined with XPS and in the bulk with FTIR. Fig. 2 shows high resolution XP spectra for a 73 nm film (film EM1) deposited with TEMAHf and H<sub>2</sub>O. The C 1s and O 1s regions are presented for the as-deposited, 500, 700 and 900 °C annealed samples. The peaks were deconvoluted using Gaussian functions. The C 1s peak at 285 eV, attributed to adventitious carbon and C–H bonds, was used to determine the full width at half maximum (FWHM) of the Gaussian singlet peak at 1.7 eV. In addition to the peak at 285 eV, the C 1s region shows a high binding energy tail and a well-resolved peak at 289 eV. This portion of the spectrum can be fitted with two Gaussian peaks, centered at 286.9 and 289 eV that correspond to C–O containing species such as C–O–H, C–O–C (286.9 eV) and O–C=O (289.0 eV) [26]. These carbon–oxygen containing species will be referred to here as carbonates. The O 1s peaks were deconvoluted using two Gaussian peaks (FWHM = 1.7 eV), centered at 530.1 eV (O–Hf) and 532.1 eV (OH–Hf, Hf–O–C) [27]. Anneals at 500 °C leave the peak intensity practically unchanged for both the C 1s and O 1s regions. A further increase in the anneal temperature at 700 and 900 °C results in gradual decrease of the impurity peak intensity in both regions, although the effect is more pronounced in the O 1s secondary peak at 532.1 eV.

The impurity peak assignment can be corroborated by FTIR measurements. Fig. 3 shows infrared absorbance data for film EM1. Spectra are presented for the as-deposited film, taken shortly after

**Table 1**  
Composition of HfO<sub>2</sub> ALD films.

	Hf at.%	O at.%	C at.%	O/Hf
TEMAHf + H <sub>2</sub> O	33 ± 3	64 ± 5	2.9 ± 0.3	1.9 ± 0.2
TDMAHf + H <sub>2</sub> O	30. ± 3	67 ± 5	3.0 ± 0.3	2.2 ± 0.2

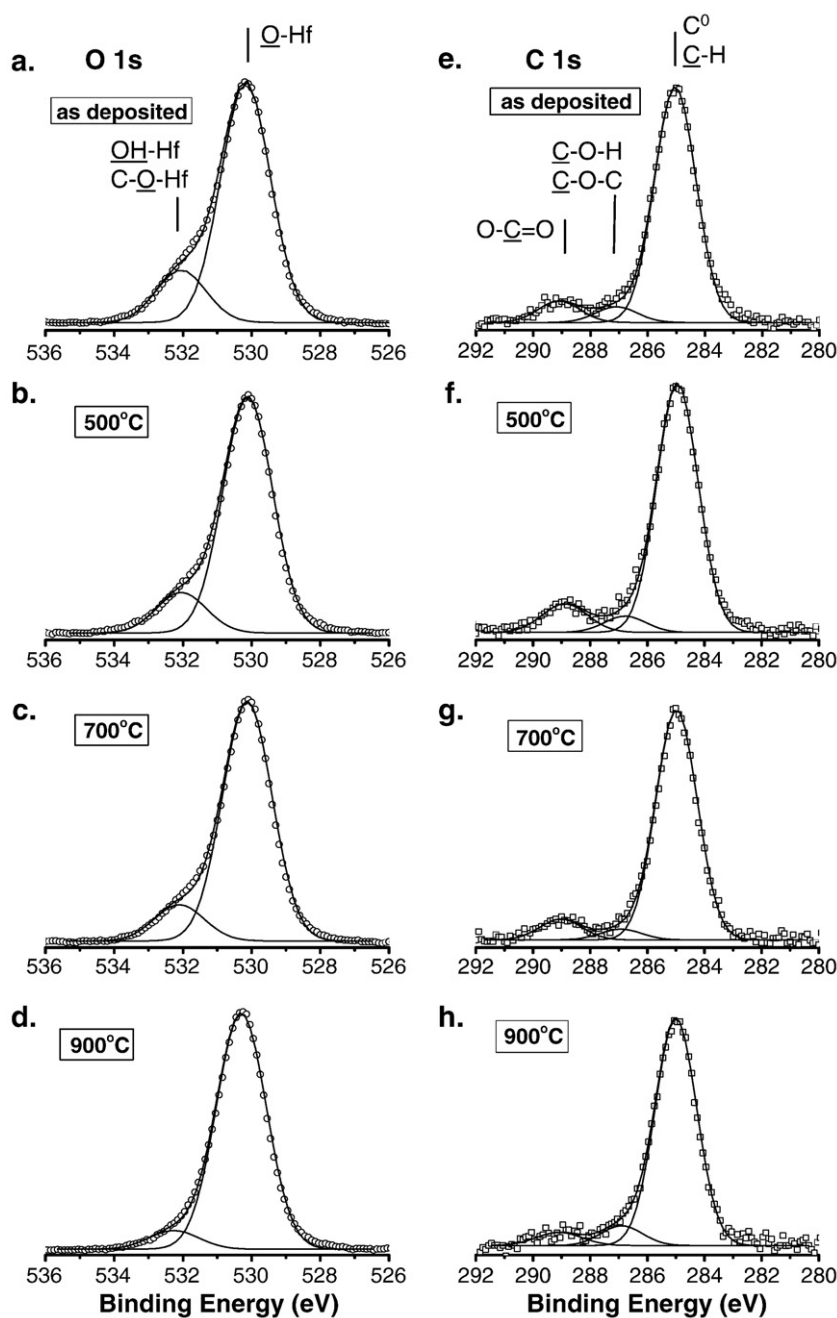


Fig. 2. O 1s (a through d) and C 1s (e through h) high resolution XP spectra for a 73 nm (600 cycles) HfO<sub>2</sub> film grown from TEMAHf and H<sub>2</sub>O. Inert anneals in Ar for 2 min result in desorption of the OH and some of the carbonate species bonded in the film.

deposition and after a 900 °C Ar anneal. For the as-deposited film, the infrared spectrum exhibits well-resolved peaks at 1200–1800 cm<sup>-1</sup> and 2800–3050 cm<sup>-1</sup>. The well-resolved peaks in the range of 1200–1800 cm<sup>-1</sup> are associated mostly with absorptions from different carbonate species [28–30]. The broad peak at 2900–3800 cm<sup>-1</sup> result from H<sub>2</sub>O molecules adsorbed in the film and surface H-bonded OH species and the strong peak at 3731 cm<sup>-1</sup> is due to terminal OH species [31,32]. The faint peaks at 2800–3050 cm<sup>-1</sup> are attributed to the presence of C–H bonding [33]. The 900 °C anneal removes most of the OH associated species but fails to remove the majority of the carbonates in agreement with the XPS results.

XPS and FTIR measurements indicate that the major impurities in the TEMAHf films are bulk H<sub>2</sub>O and terminal OH species as well as bonded carbon in the form of carbonate species. The FTIR data indicate

that the terminal OH species are more persistent than the bulk OH as there is some intensity remaining at 3731 cm<sup>-1</sup> even after anneals at 900 °C. Similarly, only a small decrease in the intensity of the carbonate species is observed after anneals at 900 °C. Based on those results, the main contribution to the secondary high binding energy peak in the O 1s XP spectrum (Fig. 2a–d) is assigned to the presence of the Hf–OH species and the residual intensity after the 900 °C anneal is assigned to the presence of terminal OH species and Hf–O–C bonding. Similarly, the temperature evolution of the C 1s spectra indicate that the residual intensity after the 900 °C anneal is probably due to C–O–C (286.9 eV) and O–C=O (289.0 eV) type bonding. Deviation in the fractional reduction of the impurity peak intensities between the XPS and FTIR measurements is not uncommon as XPS is a surface sensitive technique and FTIR is a bulk sensitive technique.

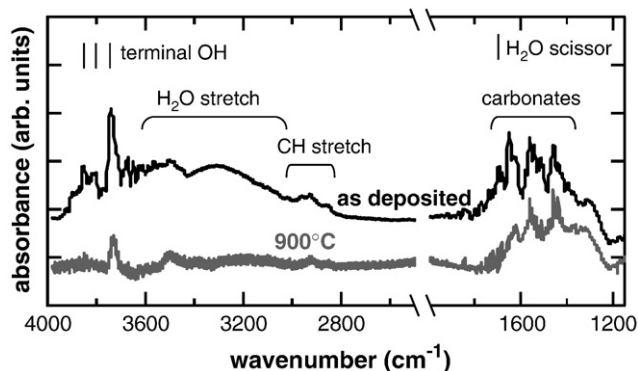


Fig. 3. FTIR transmission spectrum for the as-deposited EM1 (73 nm) film grown from TEMAHf and H<sub>2</sub>O. For the bottom spectrum the film was annealed in Ar at 900 °C for 2 min.

### 3.3. Bulk film morphology

Each ALD process was used to prepare two sets of samples see (Table 2) with thickness ~30 and ~70 nm. Pieces from these samples were RTA annealed for 2 min in Ar at temperatures ranging from 300 to 900 °C and examined using XRD and FTIR.

Fig. 4 shows XRD scans ranging from  $2\theta = 15\text{--}53^\circ$  for samples prepared from film EM1 after Ar anneals for 2 min at various temperatures. The as-deposited film shows slight structure as evidenced by two peaks at about  $28^\circ$ ,  $31^\circ$  and the beginning of a doublet at  $\sim 35^\circ$ , but is mainly amorphous as expected from the moderate ALD process temperature (the intense peak at  $\sim 28^\circ$  may also originate from the Si substrate (111) reflection). Annealing at temperatures as low as 300 °C induces a large change in the film structure attributed to the formation or growth of existing monoclinic crystallites, which are labeled according to the diffraction plane. The information regarding crystal structure is taken from the database included with the spectrometer software. Nearly all of the observed Bragg peaks may be attributed to the monoclinic polymorph, in agreement with earlier observations for similar ALD films [22,34–36]. The position of the doublet at  $35^\circ$  and at  $\sim 50^\circ$  overlaps with peaks from the tetragonal crystalline phase, but no isolated peaks from this structure are observed in the spectrum which indicates that this phase is not present. There is no significant change in structure when increasing the annealing temperature from 300–900 °C.

The sets of EM1 and EM2 samples were examined with FTIR in the far IR region and absorbance spectra from  $550\text{--}200\text{ cm}^{-1}$  are shown on Fig. 5. The as-deposited EM1 (Fig. 5a) film shows some faint structure, and there is considerable change in absorbance after annealing at 300 °C. A set of characteristic absorbance peaks appears after annealing at the same temperature that produces structure in the XRD patterns. Similar to the trend observed in the XRD data, there is no significant change in structure or peak intensity when the temperature is increased from 300–900 °C. The samples derived from film EM2 (Fig. 5b) exhibit a broad amorphous background without any apparent structure for anneal temperatures up to 500 °C. Between 500–600 °C there is a transition to the crystalline phase,

Table 2

Deposition chemistry, thickness and starting surface for some of the HfO<sub>2</sub> films examined in this work.

Sample name	Precursor	Deposition temperature (°C)	SE Thickness (nm)	Starting surface
EM1	TEMAHf	250	73	Si–OH
EM2	TEMAHf	250	33	Si–H
DM1	TDMAHf	275	76	Si–H
DM2	TDMAHf	275	33.5	Si–H

The film thickness was measured by SE.

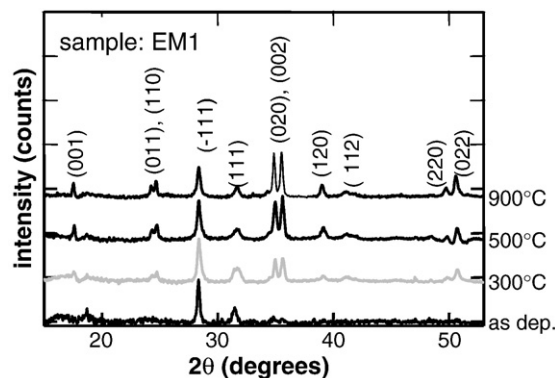


Fig. 4. XRD data for the as-deposited and RTA annealed in Ar for 2 min at 300, 500 and 900 °C EM1 film. Crystallization is detected in the as-deposited film and enhanced by the thermal treatment.

again marked by sharp absorbance peaks which are very similar to film EM1. No significant change is observed for anneal temperatures from 600 to 900 °C.

Two sets of TDMAHf samples, produced from films DM1 and DM2, were subjected to the same annealing procedure as the TEMAHf films. XRD patterns from both sets of samples are displayed on Fig. 6. Fig. 6a shows a large amount of structure present in the as-deposited DM1 film which again is attributed to crystallization in the monoclinic phase. The doublet at  $\sim 50^\circ$  becomes more defined after a 700 °C anneal, with no significant variation after that. Film DM2 (Fig. 6b) remains amorphous for anneals up to 600 °C. At 600 to 700 °C there is a transition from the amorphous to crystalline phase, characterized by a series of Bragg peaks which correspond to the monoclinic phase and are marked by the diffraction plane. The strong line at  $\sim 28^\circ$  also corresponds to a Si (111) reflection, and a subtle peak at  $\sim 48^\circ$  corresponds to the Si substrate (220) plane. There is no noticeable

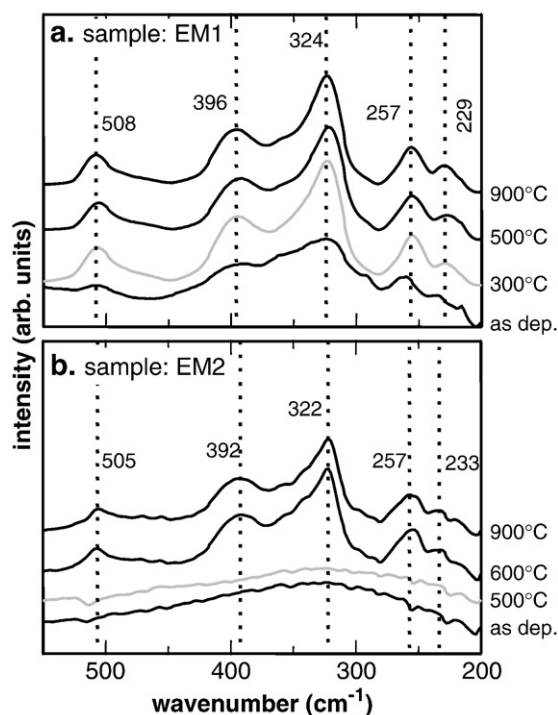


Fig. 5. Far IR absorbance spectra for films EM1 and EM2. For the thicker EM1 film (73 nm) the spectrum of the as-deposited piece shows some structure, indicative of crystallization, that intensifies after anneals. The spectrum for the thinner EM2 film (33 nm) remains structureless for anneals up to 500 °C and displays well defined peaks indicative of film crystallization for anneals at 600 °C and above.

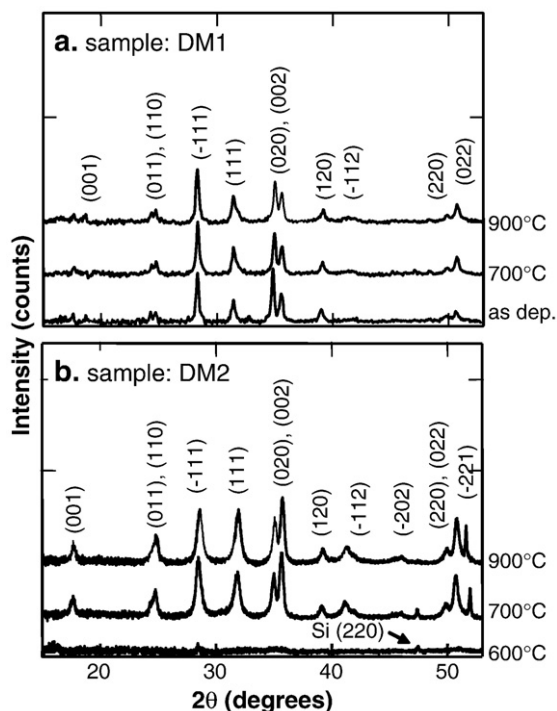


Fig. 6. XRD scans for the as deposited and RTA annealed in Ar for 2 min DM1 and DM2 films. For the thicker DM1 film (76 nm) crystallization is detected in the as-deposited film. The thinner DM2 film (33.5 nm) remains amorphous for anneals up to 600 °C.

change in structure for temperatures above 700 °C. Similarly to the TEMAHf films, thicker films (~70 nm) are more susceptible to crystallization at low anneal temperatures.

The same films that were used for XRD analysis were also examined with FTIR, and the normalized absorbance spectra for the range of 550–200 cm<sup>-1</sup> are shown in Fig. 7. The as-deposited DM1 film in Fig. 7a displays some structure, but the characteristic peaks are fairly broad. The peaks become sharper after annealing at 700–900 °C, corroborating the slight increase in intensity of the corresponding XRD patterns (Fig. 6a). The absorbance spectrum for film DM2 is broad and structureless for anneals below 600 °C. At 700 °C a series of well-defined peaks superimposed on the amorphous background appear and their position is marked by the vertical dashed lines. Similar to the trend of the XRD data, there is no significant change in the peak structure from 700–900 °C.

Figs. 4–7 demonstrate an interesting correlation between XRD and FTIR spectra; both techniques can be used for the detection of crystallization in sufficiently thick films, although XRD additionally offers the capability to determine the crystallization phase. This relationship between infrared absorbance spectra and XRD patterns has been observed before with HfO<sub>2</sub> films grown by RF sputtering (monoclinic phase), [37] plasma ion assisted deposition (cubic), [38] TDMAHf/H<sub>2</sub>O (monoclinic), [21] and TDEAHf/O<sub>3</sub> (monoclinic) [39]. There is very little information available regarding the vibrational modes in crystalline HfO<sub>2</sub>. A density-functional theory study on the structure of different crystalline phases of HfO<sub>2</sub> was performed by Zhao and Vanderbilt, where they identify 19 total active IR modes in the monoclinic, tetragonal, and cubic crystal phases [40]. Some of the vibrational modes that we observe in the far-IR region, namely the absorbance peaks at 393 cm<sup>-1</sup> and 256 cm<sup>-1</sup> are in good agreement with their results for the monoclinic phase. A number of absorbance peaks could overlap, so this is certainly a qualitative comparison. The calculations of Zhao and Vanderbilt are performed for single crystal structures whereas the samples used in this work are polycrystalline. This difference may account for the shifts in the frequency of some peaks.

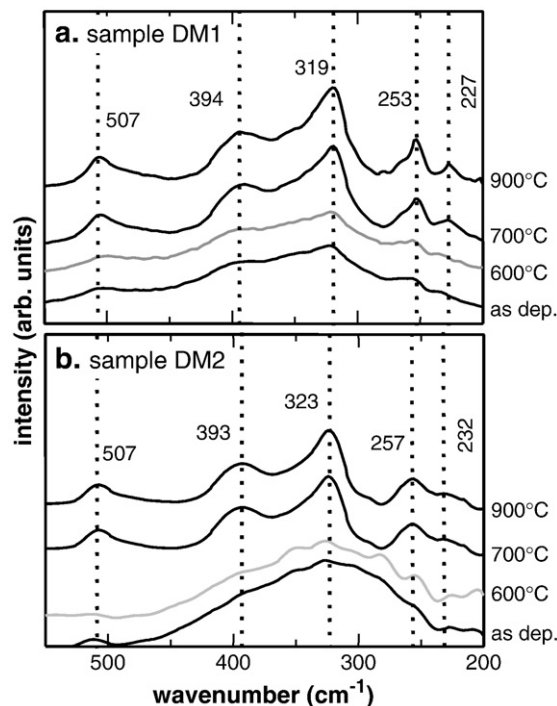


Fig. 7. Far IR absorbance spectra for films DM1 and DM2. For the thicker DM1 film the spectrum of the as-deposited piece shows some structure, indicative of crystallization, that intensifies after anneals. The spectrum for the thinner DM2 film begins to show signs of crystallization for anneals at 600 °C.

The crystallization threshold temperature for the films appears to depend on film thickness. Films that are ~30 nm thick remain amorphous up to annealing temperatures of 600 °C (EM2 and DM2), while ~70 nm thick as-deposited films (EM1 and DM1) display some degree of crystallization. This effect is well-described in a model by Hausmann and Gordon for HfO<sub>2</sub> and ZrO<sub>2</sub> film crystallization during ALD growth [36]. According to the model, a crystal nucleation event may occur at any point during the ALD process, and the probability of such an event increases with temperature. Afterwards, crystallite growth proceeds both laterally and vertically but is favored in the vertical direction. Therefore, a longer deposition provides more opportunity for crystallite nucleation, and more time and space for the crystals to grow. This may explain the reason crystallization is detected in the as-deposited ~70 nm thick samples (EM1 and DM1). In the ~30 nm thick films (EM2 and DM2) the crystallites may be too small to be detected with FTIR or XRD.

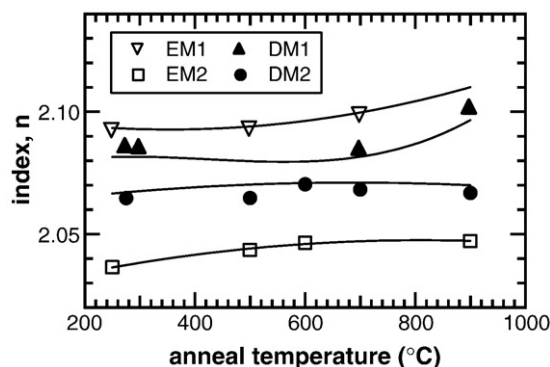
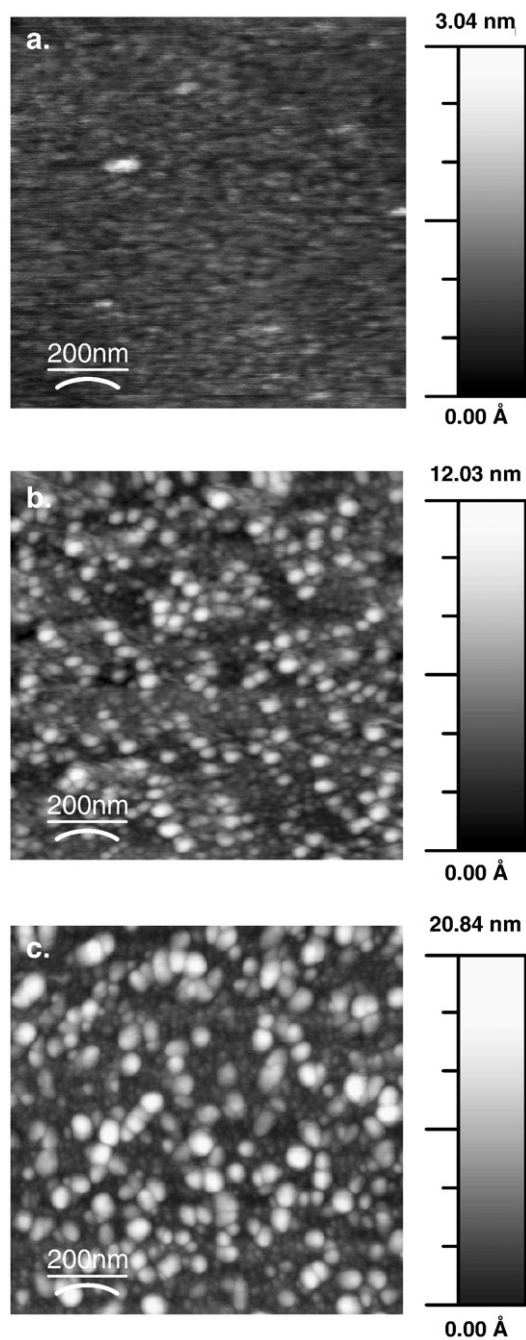


Fig. 8. The index of refraction at 540 nm for as deposited and post deposition inert annealed (Ar, 2 min) HfO<sub>2</sub> films. For all samples the measured value is very close to that of bulk crystalline HfO<sub>2</sub> and similar ALD HfO<sub>2</sub> films. The solid lines are intended as a guide to the eye.



**Fig. 9.** AFM images for a series of films deposited from TEMAHf + H<sub>2</sub>O on native oxide Si surfaces. The film thickness and rms roughness is (a) 12 nm, 0.2 nm, (b) 43 nm, 1.6 nm and (c) 73 nm, 3.5 nm respectively.

### 3.4. Index of refraction

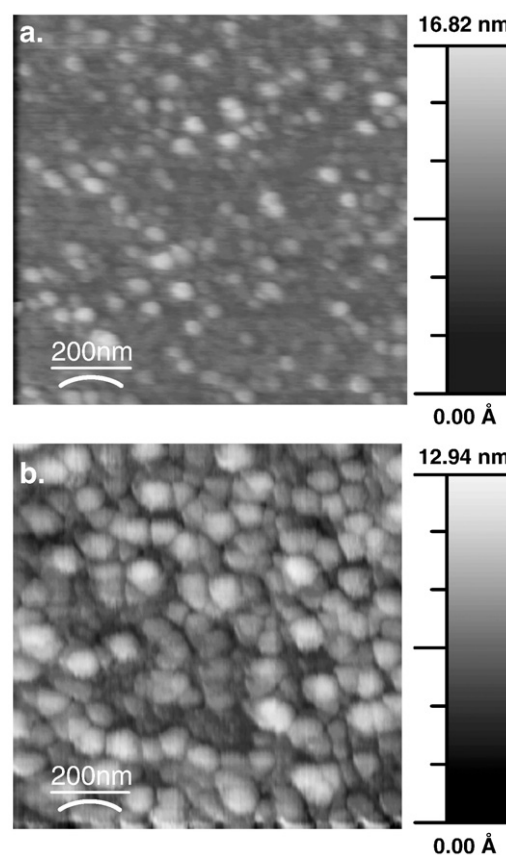
Fig. 8 displays measurements of the film refractive index,  $n$ , at 540 nm as a function of post deposition anneal temperature for the EM1, EM2, DM1 and DM2 sample sets. The same pieces of the samples used for the FTIR, XRD and AFM measurements were used to obtain this data set as well. The index of refraction for each set of films appears practically independent of the post deposition treatment temperature and ranges from 2.04 to 2.1, very close to the bulk value of 2.1 and in good agreement with the refractive indices reported for similar HfO<sub>2</sub> ALD films [20–22]. The measured refractive index of the films is very close to the bulk value and exhibits at best a very weak dependence on post deposition anneal temperature. ALD films, in

general, are fairly smooth and dense even without further thermal treatment and as a result exhibit refractive indices close to the bulk values. A combination of ellipsometry and Rutherford back scattering data indicate that the as-deposited films for both processes have ~85–95% the density of crystalline HfO<sub>2</sub> depending on the starting surface [2,41]. The thicker films exhibit somewhat higher indices of refraction as their structure is closer to that of bulk HfO<sub>2</sub>.

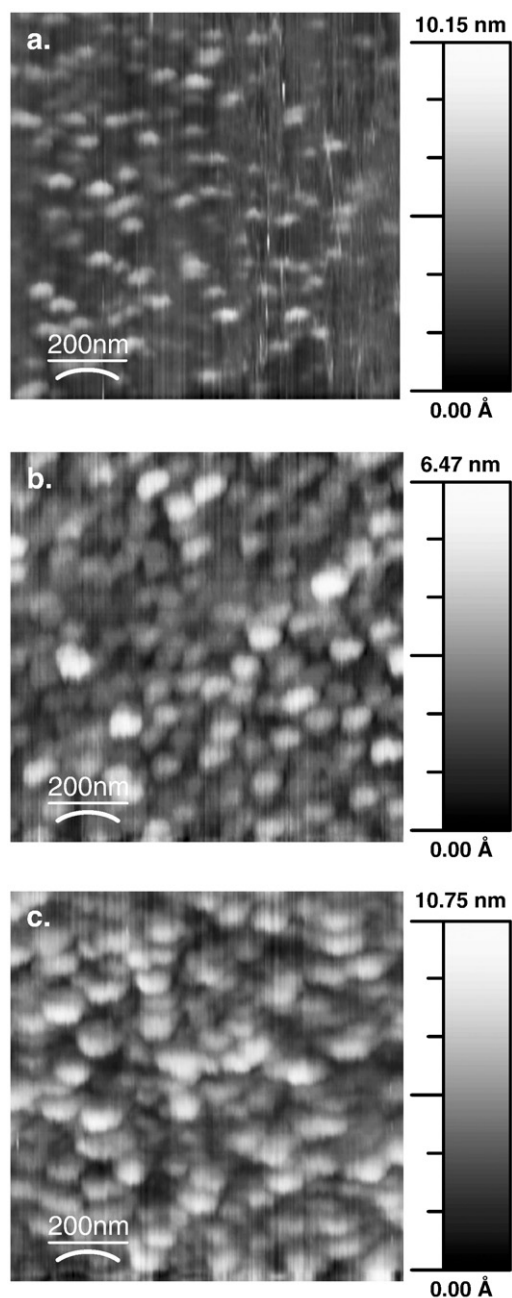
### 3.5. Surface film morphology

Fig. 9 shows AFM data for a series of TEMAHf films with thickness 12 nm (Fig. 9a), 43 nm (Fig. 9b), and 73 nm (Fig. 9c) deposited on native oxide Si surfaces. The root mean square (rms) roughness for these films is 0.2 nm, 1.6 nm and 3.5 nm respectively and it increases with film thickness both in terms of absolute value and as percentile of the film thickness. (1.7, 3.7, and 4.8% of the film thickness respectively). The surface of the thinnest film, is very smooth without any distinguishable features. The surface of the 43 nm film displays scattered particles of ~40 nm in size. The number and size of these particles increases for the thickest film (73 nm). These particles may correspond to minute crystallites in the film that are seeded during the deposition process. Fig. 10 shows the evolution of the surface features for sample EM2 (33 nm film deposited on Si–H) after anneals at 500 °C (Fig. 10a) and 900 °C (Fig. 10b). The particle density and size increases from ~30 nm at 500 °C to ~80 nm after a 900 °C treatment (Fig. 10b). Based on the XRD and FTIR data the film is amorphous at 500 °C and has crystallized at 900 °C.

Fig. 11 shows the evolution of the surface features for sample DM2 (33.5 nm film deposited on Si–H) after high temperature inert anneals at 400 °C (Fig. 11a), 700 °C (Fig. 11b), and 900 °C (Fig. 11c). The number density and size of the formed particles increases with the thermal



**Fig. 10.** AFM images for a 33 nm film deposited from TEMAHf + H<sub>2</sub>O on Si–H surfaces (film EM2) and annealed in Ar for 2 min at (a) 500 °C and (b) 900 °C. The rms roughness is (a) 1.4 nm and (b) 1.6 nm respectively.



**Fig. 11.** AFM images for a 33.5 nm film deposited from TDMAHF + H<sub>2</sub>O on Si-H surfaces (film DM2) annealed in Ar for 2 min at (a) 400 °C and (b) 700 °C and (c) 900 °C. The rms roughness is (a) 0.9 nm (b) 0.9 nm and (c) 1.7 nm respectively.

budget. The rms roughness increases from 0.9 nm at 500 °C to 1.7 nm at 900 °C. Based on the XRD and FTIR data the film is amorphous at 400 °C and has crystallized at 700 °C.

Both ALD processes produce fairly smooth films. Films around 10 nm do not display any appreciable surface features but thicker films ( $\geq 30$  nm) exhibit small circular surface features. The film rms roughness and the size and density of the surface features increases as a function of film thickness and post deposition anneal temperatures. The feature size enhancement occurs around the same temperature that an enhancement in the intensity of the characteristic peaks in the XRD and FTIR spectrum is observed and may indicate an increase in crystallite size. According to the aforementioned crystallite growth model by Hausmann and Gordon, the AFM images may reveal the top of HfO<sub>2</sub> crystallites protruding above the film surface [36]. Similar observations have been made for other HfO<sub>2</sub> ALD systems such as

HfCl<sub>4</sub>/H<sub>2</sub>O [27]. The surface roughness of films deposited on Si-H substrates is marginally larger than that for similar films deposited on native oxide Si but the evolution of the surface features after thermal treatments for both starting surfaces is very similar [2].

#### 4. Conclusions

The properties of HfO<sub>2</sub> films grown by ALD using the TEMAHf + H<sub>2</sub>O and TDMAHF + H<sub>2</sub>O chemistries have been examined. The two precursors belong to the same amide family and result in similar growth conditions. For TEMAHf the ALD minimum was found at 250 °C achieving a GPC of 1.2 Å/cycle while for TDMAHF the ALD minimum was found at 275 °C achieving a GPC of 1.0 Å/cycle. Common impurities detected in the films are carbonates and terminal and bulk OH. Most of the OH and part of the carbonates are desorbed after inert anneals. Film crystallization is found to depend on the film thickness; thicker HfO<sub>2</sub> films crystallize at lower temperatures, and predominantly in the monoclinic phase. Films are fairly smooth with the rms roughness increasing with film thickness and post deposition treatment temperature. There is excellent correlation in the appearance of well resolved peaks in the far IR spectrum of HfO<sub>2</sub> with film crystallization as detected by XRD. The index of refraction for all films is very close to that for bulk crystalline HfO<sub>2</sub> and appears to be affected very weakly by post deposition thermal treatment.

#### Acknowledgments

Acknowledgments are made to the Donors of the American Chemical Society Petroleum Research Fund and the UMBC ADVANCE Institutional Transformation Program (NSF-0244880) for partial support of this work.

#### References

- [1] J. Lu, J. Aarik, J. Sundqvist, K. Kukli, A. Harsta, J.-O. Carlsson, *J. Cryst. Growth* 273 (3–4) (2005) 510.
- [2] J.C. Hackley, T. Gougousi, J.D. Demaree, *J. Appl. Phys.* 102 (2007) 034101.
- [3] Y.C. Chang, M.L. Huang, K.Y. Lee, Y.J. Lee, T.D. Lin, M. Hong, J. Kwo, T.S. Lay, C.C. Liao, K.Y. Cheng, *Appl. Phys. Lett.* 92 (7) (2008) 072901.
- [4] A. Delabie, R.L. Puurunen, B. Brijis, M. Caymax, T. Conard, B. Onsia, O. Richard, W. Vandervorst, C. Zhao, M.M. Heyns, M. Meuris, M.M. Viitanen, H.H. Brongersma, M. de Ridder, L.V. Goncharova, E. Garfunkel, T. Gustafsson, W. Tsai, *J. Appl. Phys.* 97 (2005) 064104.
- [5] D.A. Neumayer, E. Cartier, *J. Appl. Phys.* 90 (4) (2001) 1801.
- [6] K. Yamamoto, S. Hayashi, M. Kubota, M. Niwa, *Appl. Phys. Lett.* 81 (11) (2002) 2053.
- [7] P. Chen, H.B. Bhandari, T.M. Klein, *Appl. Phys. Lett.* 85 (9) (2004) 1574.
- [8] L. Gallais, J. Capoulade, J.-Y. Natoli, M. Commandré, M. Cathelinaud, C. Koc, and M. Lequime *Appl. Opt.* 47 (10) (2008) C107.
- [9] R. Chow, S. Falabella, G.E. Loomis, F. Rainer, C.J. Stolz, *Appl. Opt.* 32 (1993) 5567.
- [10] P. André, L. Poupinet, G. Ravel, *J. Vac. Sci. Technol. A* 18 (2000) 2372.
- [11] P.Y. Hou, J. Stringer, *J. Electrochem. Soc.* 138 (1) (1991) 327.
- [12] S. Shimada, T. Aketo, *J. Am. Ceram. Soc.* 88 (4) (2005) 845.
- [13] S.V. Volkov, A.V. Grafov, G.A. Battiston, L.A. Koval, R. Gerbasi, M. Porchia, P. Zanella, E.A. Mazurenko, in: M.D. Allendorf, C. Bernard (Eds.), *Chemical Vapor Deposition: CVD XIV and EUROCVD-11*, Electrochemical Society, Paris, 1997, p. 455.
- [14] M.F. Al-Kuhaili, *Opt. Mater.* 27 (3) (2004) 383.
- [15] J.M. Khoshmana, M.E. Kordesch, *Surf. Coat. Technol.* 201 (6) (2006) 3530.
- [16] X. Liu, S. Ramanathan, A. Longdergan, A. Srivastava, E. Lee, T.E. Seidel, J.T. Barton, D. Pang, R.G. Gordon, *J. Electrochem. Soc.* 152 (2005) G213.
- [17] M. Ritala, M. Leskelä, in: H.S. Nalwa (Ed.), *Handbook of Thin Film Materials*, vol. 1, Elsevier, Amsterdam, 2002, p. 103.
- [18] D.M. Hausmann, E. Kim, J. Becker, R.G. Gordon, *Chem. Mater.* 14 (2002) 4350.
- [19] I. Horcas, R. Fernandez, J.M. Gomez-Rodriguez, J. Colchero, J. Gomez-Herrero, A.M. Baro, *Rev. Sci. Instrum.* 78 (2007) 013705.
- [20] K. Kukli, M. Ritala, T. Sajavaara, J. Keinonen, M. Leskela, *Chem. Vap. Deposition* 8 (2002) 199.
- [21] K. Kukli, T. Pilvi, M. Ritala, T. Sajavaara, J. Lu, M. Leskela, *Thin Solid Films* 491 (2005) 328.
- [22] D.H. Triyoso, R.I. Hegde, B.E. White Jr., P.J. Tobin, *J. Appl. Phys.* 97 (2005) 124107.
- [23] A. Deshpande, R. Inman, G. Jursich, C. Takoudis, *J. Vac. Sci. Technol. A* 22 (2004) 2035.
- [24] B.D. Ratner, D.G. Castner, in: J.C. Vickerman (Ed.), *Surface Analysis: the principle techniques*, Wiley, West Sussex, 1997, p. 66.
- [25] T. Gougousi, G.N. Parsons, *J. Appl. Phys.* 95 (3) (2004) 1391.
- [26] B.D. Ratner, D.G. Castner, in: J.C. Vickerman (Ed.), *Surface Analysis: the principle techniques*, Wiley, West Sussex, 1997, p. 51.

- [27] D. Triyoso, R. Liu, D. Roan, M. Ramon, N.V. Edwards, R. Gregory, D. Werho, J. Kulik, G. Tam, E. Irwin, X.-D. Wang, L.B. La, C. Hobbs, R. Garcia, J. Baker, B.E. White Jr., P. Tobin, *J. Electrochem. Soc.* 151 (10) (2004) F220.
- [28] G. Busca, V. Lorenzelli, *Mater. Chem.* 7 (1982) 89.
- [29] S. Bernal, J.A. Diaz, R. Garcia, J.M. Rodriguez-Izquierdo, *J. Mater. Sci.* 20 (1985) 537.
- [30] T. Gougousi, D. Niu, R.W. Ashcraft, G.N. Parsons, *Appl. Phys. Lett.* 83 (2003) 3543.
- [31] M.P. Rosynek, D.T. Magnuson, *J. Catal.* 46 (1977) 402.
- [32] A.A. Tsyganenko, V.N. Filimonov, *J. Mol. Struct.* 19 (1973) 579.
- [33] J. Kondo, H. Abe, Y. Sakata, K. Maruya, K. Domen, T. Onishi, *J. Chem. Soc., Farad. Trans. 1* 84 (2) (1988) 511.
- [34] K. Kukli, M. Ritala, T. Sajavaara, J. Keinonen, M. Leskelä, *Thin Solid Films* 416 (2002) 72.
- [35] K. Kukli, M. Ritala, J. Lu, A. Harsta, M. Leskela, *J. Electrochem. Soc.* 151 (2004) F189.
- [36] D.M. Hausmann, R.G. Gordon, *J. Cryst. Growth* 249 (2003) 251.
- [37] K. Tomida, H. Shimizu, K. Kita, K. Kyuno, A. Toriumi, in: J. Morais, D. Kumar, M. Houssa, R.K. Singh, D. Landheer, R. Ramesh, R.M. Wallace, S. Guha, H. Koinuma (Eds.), *Integration of Advanced Micro- and Nanoelectronic Devices-Critical Issues and Solutions*, vol. 811, Materials Research Society, Warrendale, PA, 2004, p. D10.9.
- [38] M. Modreanu, J. Sancho-Parramon, O. Durand, B. Servet, M. Stchakovsky, C. Eypert, C. Naudin, A. Knowles, F. Bridou, M.-F. Ravet, *Appl. Surf. Sci.* 253 (2006) 328.
- [39] R. Katamreddy, R. Inman, G. Jursich, A. Soulet, C. Takoudis, *J. Mater. Res.* 22 (12) (2007) 3455.
- [40] X. Zhao, D. Vanderbilt, *Phys. Rev. B* 65 (2002) 233106.
- [41] J.C. Hackley, T. Gougousi, J.D. Demaree, *J. Vac. Sci. Technol. A* 25 (5) (2008) 1235.